Bioinspired Jet Propulsion for Disturbance Rejection of Marine Robots

Michael Krieg, Kevin Nelson, Jeremiah Eisele, and Kamran Mohseni

***Abstract*—This investigation takes the first step toward characterizing autonomous underwater vehicle (AUV) behavior trying to perform station keeping using bioinspired thrusters under the influence of disturbances with multiple amplitudes and frequencies. We describe the similarities between periodic disturbance rejection and the frequency response of the AUV performing oscillating maneuvers, and the significance of maneuvering regimes previously identified for this type of propulsion. We measured the exact position/orientation of the AUV using an underwater motion capture system and provide position data to the AUV controller in real time for feedback control. A wave disturbance generator was developed for this study in order to characterize the vehicle tracking performance in the presence of both high-amplitude low-frequency disturbances and low-amplitude high-frequency disturbances. The bioinspired maneuvering technique is demonstrated to provide adequate control capabilities for both types of disturbances maintaining in all cases position errors less than half the vehicle diameter, and proved especially adept at compensating for low-amplitude high-frequency disturbances, which can be difficult to overcome using traditional marine thrusters.**

***Index Terms*—Biologically-inspired robots, marine robotics, motion control.**

I. Introduction

BIOINSPIRED robotic systems are becoming more and more common as engineers seek to leverage advantages gained through millennia of evolution. Bioinspired designs can be particularly attractive for underwater robotic propulsion because many marine organisms have both accurate low speed maneuvering and efficient long range migration; whereas, traditional underwater robot propulsion typically attains one of those qualities at the expense of the other. Some groups have attempted to recreate the locomotion of flapping fish [1]–[3], we have instead looked into the propulsion of squid and jellyfish.

Manuscript received September 17, 2017; accepted February 5, 2018. Date of publication March 5, 2018; date of current version March 28, 2018. This letter was recommended for publication by Associate Editor M. D. Dunbabin and Editor R. Roberts upon evaluation of the reviewers' comments. This work was supported by the Office of Naval Research under Grant N00014-16-1-2083. *(Corresponding author: Michael Krieg.)*

M. Krieg is with the Department of Electrical and Computer Engineering, University of Florida, Gainesville, FL 32611 USA (e-mail: kriegm@ufl.edu).

K. Nelson and J. Eisele are with the Department of Electrical and Computer Engineering, University of Florida, Gainesville, FL 32611 USA (e-mail: kjnelson@ufl.edu; jeisele@ufl.edu).

K. Mohseni is with the Department of Mechanical and Aerospace Engineering, Department of Electrical and Computer Engineering, and Institute for Networked Autonomous Systems, University of Florida, Gainesville, FL 32611 USA (e-mail: mohseni@ufl.edu).

Digital Object Identifier 10.1109/LRA.2018.2812219

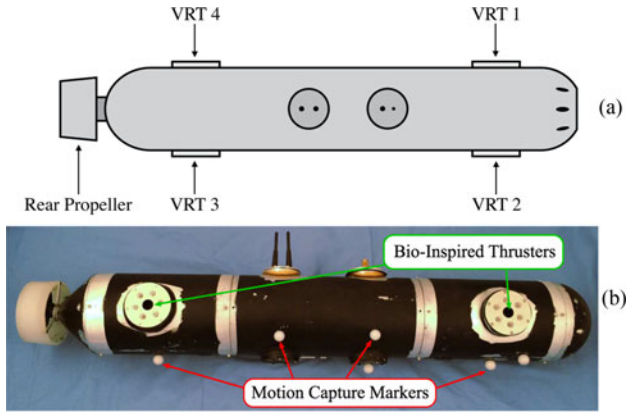

Fig. 1. (a) Diagram of CephaloBot showing the thruster locations. (b) Photo of CephaloBot with motion capture markers labeled.

We have demonstrated previously that a new type of underwater jet propulsion inspired by the locomotion of squid and jellyfish allows AUVs to provide uncoupled forces/torques in surge sway and yaw, even at zero forward speed, without external structures that increase vehicle drag [4], [5]. This capability is possible because the thruster periodically ingests and expels water jets using a flexible internal cavity. The thruster sucks in and shoots out the same amount of fluid so it has a zero net mass flux, but it has a positive net transfer of impulse and energy over a full jetting cycle. As can be seen in Fig. 1, the AUV maintains a streamlined shape since the thrusters are internal.

Due to the large density and viscosity of the surrounding fluid, currents and waves result in significant forces on marine robots. Therefore, being able to provide forces to appropriately compensate for environmental disturbances is critical in underwater engineering. Traditional propeller based thrusters have a time delay associated with reaching a given level of thrust that is inversely proportional to the level of thrust [6]. In addition, without a well established flow passing through the propeller the thrust output can exhibit large degrees of hysteresis, as is seen in thrusters oscillating at high frequencies [7]. As such, underwater robots typically have difficulty maintaining position in chaotic riverine and littoral environments. There have been several control techniques employed to improve position tracking stability for AUVs such as sliding mode controllers [6], [8] disturbance velocity estimators [9] and non-linear controllers [10].

The bioinspired thruster technology has multiple features suggesting that it should work well providing control forces

necessary to overcome chaotic disturbances. Although the thruster forces are inherently unsteady, associated with switching back and forth between jetting and refilling phases, the thruster reaches an average thrust nearly instantaneously [11]. The frequency response of an autonomous underwater system performing periodic maneuvers with the bioinspired propulsion is heavily dependent on the ratio of vehicle length scale to maneuver length scale [11]. Furthermore it is indicated that the bioinspired jet propulsion is ideally suited for maneuvers in the *Docking* regime, which are characterized by maneuvers with length scale smaller than the vehicle length scale. In the current study, we investigate the position tracking stability of an underwater robot in the presence of disturbances of various magnitudes. Specifically, we look into the relationship between disturbance rejection and maneuvering regime dynamics.

Section II gives a description of the AUV and the bioinspired thruster technology, then provides a summary of the maneuvering regime analysis. In Section III the experimental equipment and procedures are described, including the underwater motion capture system and disturbance generator. Section IV reports and analyzes the AUV position tracking results for the different disturbance types, and the work is concluded in Section V.

II. AUV Dynamics and Control

A. Vehicle and Thruster Description

The AUV used in this experiment, named CephaloBot, is a slender torpedo shaped vehicle, 1120 mm in length and 150 mm in diameter, with a mass of 20 kg. The AUV is shown in Fig. 1 and was described in great detail in [5]. The AUV has a propeller in the rear for forward propulsion and four squid inspired thrusters to provide maneuvering control forces for yaw and sway.

The maneuvering thrusters, similar to squid and jellyfish, create propulsive forces by ingesting and expelling jets of water from a flexible cavity. The flexible thruster cavity that creates the jet flow is internal to the vehicle hull so that maneuvering forces can be generated without sacrificing a slender hydrodynamic body shape. The layout of the thruster inside the vehicle hull is illustrated in Fig. 2.

The thrust output of the device is inherently unsteady. Since propulsive jets are created from a finite volume of fluid within an internal cavity, the jet flow must be periodically terminated in order to refill the cavity, resulting in the unsteady jetting process. While the unsteady propulsion affects the frequency response of the maneuvering system, the large inertia of the vehicle relative to the mass of each jet minimizes any oscillations in vehicle velocity during operation. The unsteady nature of the jetting also results in vortex ring formation which significantly affects the thrust dynamics.

At the start of each jetting cycle the ejected fluid forms a shear layer with an unstable free end that rolls into a vortex ring at the front of the jet. It is known that the formation of this leading edge vortex ring plays a critical role in the locomotion of jellyfish [12] and squid [13]. Therefore the output of this type of thruster is sensitive to both the geometry/operating conditions of the thruster, as well as the dynamics associated with vortex

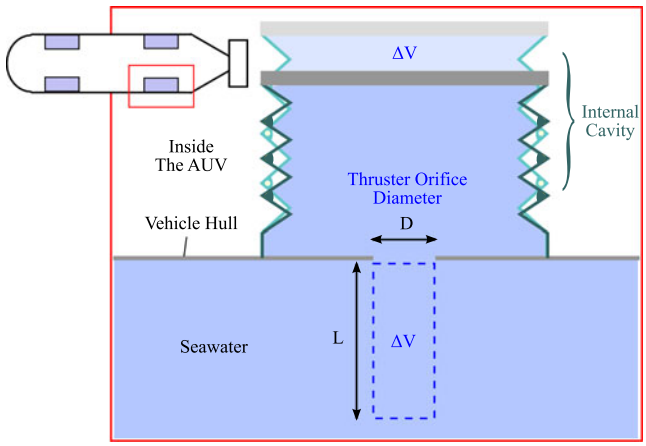

Fig. 2. Schematic diagram of the bioinspired underwater thruster inside the vehicle hull.

ring formation in the expelled jet. As a first order approximation, the thrust produced at any instant can be modeled as the rate at which hydrodynamic impulse I is generated in the jet [14],

$$\frac{dI}{dt} = \frac{\rho\pi}{4} u_j^2 D^2 \left(g + \frac{k_2^\star - k_1^\star}{4} \right) . \tag{1}$$

Here ρ is the fluid density, u_j is the jet velocity, D is the Diameter of the nozzle/orifice, g is a parameter related to the axial velocity profile at the nozzle, $k_1^\star$ is the non-dimensional slope of the radial velocity profile, and $k_2^\star$ is the slope of the radial velocity gradient. The terms g, $k_1^\star$, and $k_2^\star$ are determined by the thruster geometry and vortex ring formation dynamics as laid out in [14]. It should be noted that the instantaneous forces produced by the thruster are not exactly equal to the rate of impulse generated in the jet due to pressure forces associated with accelerating/decelerating fluid inside the thruster cavity [15]. However, these forces are cyclical, so that they do not affect the average thrust over an entire pulsation cycle, but they do have a net effect on the work required to generate the propulsive jet [15].

The thrusters on CephaloBot are designed to produce jets with a stroke ratio of ≈ 3 so that they will form a single vortex ring, even in the presence of a co-flow due to vehicle motion, which has the effect of reducing the formation number [16].

B. Maneuvering Regimes and Disturbance Rejection

In order to characterize and model the control bandwidth of this type of bioinspired jetting propulsion, Krieg & Mohseni [11] investigated a virtual AUV with a single degree of freedom (sway) oscillating back and forth at different frequencies and amplitudes. By virtual vehicle we mean that the vehicle dynamics and trajectory were numerically simulated using forces measured from a prototype thruster in a static testing setup as real-time input to the simulation [11]. This study identified 3 different maneuvering regimes with fundamentally different dynamics, based on the ratio of the maneuvering amplitude to the vehicle length scale, $A^\star$. The *docking* regime consists of maneuvers smaller than the vehicle characteristic length scale, which for sway and yaw maneuvers is the AUV diameter. The

cruising regime consists of maneuvers larger than the vehicle length scale, and the *transition* regime consists of maneuvers with amplitude similar to the vehicle length scale. A linear time-invariant (LTI) model of the system was developed to account for the periodic nature of the thrust output as well as the fast response associated with reaching a steady average thrust, and approximated trim conditions based on the different maneuvering regimes.

The model accurately predicted the frequency response of the system in the *docking* and *transition* regimes, as well as the cut-off frequency of the *cruising* regime, but the frequency response of the system in the *cruising* regime at frequencies far from the cutoff frequency was not well captured due to non-linearities in the vehicle dynamics. Furthermore, given the fast transient behavior of the average thrust, the system was observed to have a relatively high control bandwidth in the docking regime, approximately 0.19 Hz for the vehicle and thruster scaling in that paper. This suggests that the bioinspired propulsion is adept at maneuvers requiring a high oscillation frequency and low oscillation amplitudes. This is a regime where traditional propeller thrusters encounter some issues. Small maneuvering amplitudes, or small thrust amplitudes, require low rotational velocities, which are associated with long time scales to reach a steady state thrust [6]. In addition, the result of higher frequency oscillations in propeller rotational speed is that a steady flow cannot be established before the propeller changes direction. This is evidenced by the significant hysteresis in [7, Fig. 9(d)]. For this particular oscillation in rotational speed the produced thrust can be in the wrong direction for more than half the speed range.

Ocean environments are characterized by current/wave disturbances over a wide range of frequencies and amplitudes [17], [18]. it is straightforward to imagine that there is a similarity between the behavior of an AUV system moving back and forth in a stationary fluid and a system trying to maintain a stationary position in an oscillating flow under an equivalent disturbance amplitude and frequency. For large scale wave/current amplitudes the uncontrolled AUV can be considered a tracer that moves with the flow so an equivalent disturbance rejection regime should be able to be identified by the parameter $A^\star$ replacing the maneuver amplitude with the wave amplitude. For smaller amplitude disturbances, the vehicle inertia will have a larger affect on the disturbance-vehicle interaction, causing some of the wave to flow over the vehicle rather than moving with it, and such a simple substitution will not be adequate. This investigation takes the first step towards characterizing AUV behavior trying to perform station keeping using bioinspired thrusters under the influence of disturbances with a range of amplitudes and frequencies.

C. Station Keeping Controller Design

The AUV used to test disturbance rejection capabilities of bioinspired thrusters uses a basic PID position error feedback controller, where the vehicle states are determined in real-time using an underwater motion capture system. In this section we describe the control algorithm and the motion capture system is described in Section III.

Station keeping is a fundamental robotic behavior necessary for a variety of missions. When designing the station keeping controller, we assume that the vehicle is roll and pitch stable. Under this assumption, the transformation matrix from the inertial frame of reference to the body frame of reference reduces to a rotation about the z axis. We also assume that the position in the inertial frame and the Euler angles of the vehicle can be accurately measured using a motion capture system. For the purposes of controller design, we will require station keeping error in the sway direction to have an rms average less than the AUV diameter. However, we would like to avoid focusing in on any single specific application, and instead investigate disturbance rejection capabilities of the bioinspired maneuvering system in general.

We developed a PID controller to asymptotically stabilize the x, y, and yaw states. The position error in the inertial frame is defined as

$$e(t) = \eta_d(t) - \eta(t). \tag{2}$$

where $e(t) = [e_x, e_y, e_\psi]^T$, $\eta = [x, y, \psi]^T$, in which x and y are positions in the global frame and ψ is the yaw angle of the rigid body, and η_d is the desired position/orientation.The PID feedback equation is:

$$\tau_c = K_p e + K_d \dot{e} + K_i \int_0^t e dt \tag{3}$$

where $\tau_c = [F_x, F_y, \tau_\psi]^T$ is a vector of forces and moments in the inertial frame and the PID control gains are defined as $K_p = \text{diag}(k_{px}, k_{py}, k_{p\psi})$, $K_d = \text{diag}(k_{dx}, k_{dy}, k_{d\psi})$, and $K_i = \text{diag}(k_{ix}, k_{iy}, k_{i\psi})$. The feedback control forces, τ_c, are then mapped to input signals to the thrusters. Since the surge, sway, and yaw dynamics are decoupled, the PID gains for each state can be tuned independently.

For this study we focus on both disturbances and position tracking dynamics mainly restricted to the sway direction. The control gains in this direction are set to $k_{py} = 5$ kg/s^2, $k_{dy} = 1.25$ kg/s, and $k_{iy} = 0.5$ kg/s^3. These control gains were selected with a basic vehicle simulation using drag and added mass coefficients that were validated for CephaloBot in [19]. The gains were then fine tuned during preliminary vehicle testing. However, we will not go into the details of that preliminary testing process because the goal of this letter is to illustrate the disturbance rejection capabilities of the bioinspired maneuvering technology, rather than characterize the effectiveness of a standard PID controller.

III. Experimental Setup

The AUV testing environment consists of a large testing tank, a motion capture system, and a wave disturbance generator. The tank, which is shown in Fig. 3, is 7.6 m in diameter, 4.6 m deep and holds 227 kl of water. The tank has an aluminum platform running across the top which allows physical access to the water, and is used to mount various testing equipment including the disturbance generator. In the following sections we describe the motion capture system and disturbance generator, respectively, in greater detail.

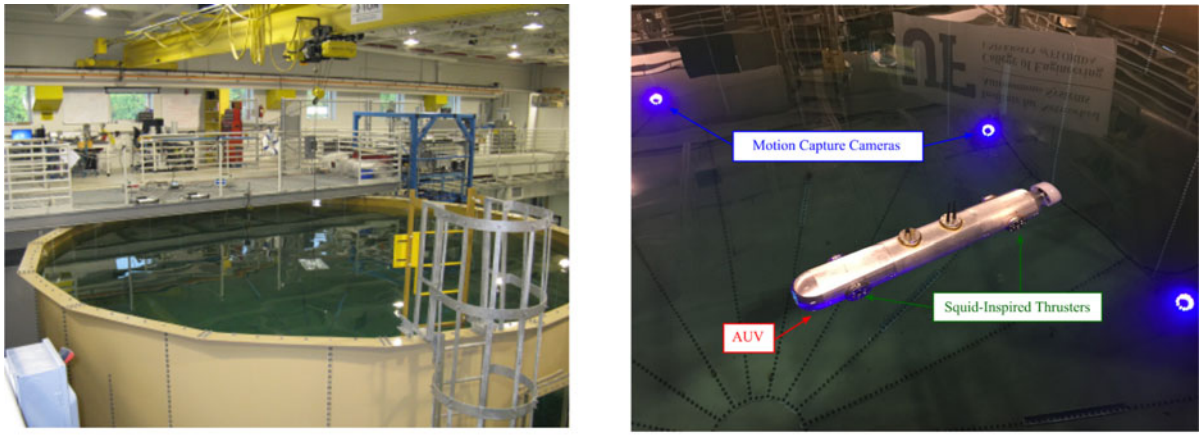

Fig. 3. Large water tank used to test AUV prototypes, showing the underwater motion capture system.

A. Real-Time Motion Capture Trajectory Feedback

Our group's motion capture system consists of six underwater Qualisys OQUS cameras, and a software package, the Qualisys Track Manager (QTM), that converts the cameras visual information to spatial measurements. The motion capture system is incorporated into our group's underwater vehicle testing tank, and is capable of tracking multiple six degree of freedom (6 DOF) rigid bodies and determining their position and attitude in real time.

Though our group has used the motion capture system in several projects involving CephaloBot [19], [20], data from the system has been extracted in post-processing. Since this project required state estimates to provide feedback for closed-loop control of CephaloBot, it was necessary to acquire the states in real-time. To improve the QTMs ability to distinguish between actual and false markers, the marker type was changed from two-dimensional circular markers to three-dimensional spherical markers, as shown in Fig. 1. Additionally, the QTM settings were adjusted to filter out any markers of the wrong size.

B. Disturbance Generation

In this experiment wave disturbances are generated by oscillating a large flat plate in the water to generate waves that impact the vehicle. A schematic of this mechanism is shown in Fig. 4. As can be inferred from the geometry of the mechanism, it creates a coupled heaving/pitching motion of the plate. These motions cannot be actuated independently, but by alternating the location of the pivot point we can adjust the relationship between pitching and heaving motions. If the depth of the plate root is h_p and the angle it makes with the horizontal plane is θ, as labeled in Fig. 4, then in general the motion of the plate is described by,

$$h_p = h_0 + a\cos(\theta) + b\sin(\theta)$$
$$\theta = \frac{A_\theta}{2}\cos(2\pi f t) \tag{4}$$

where a and b are characteristic lengths shown in Fig. 4. For this experiment a and b are 914 mm (36 in) and 152 mm (6 in),

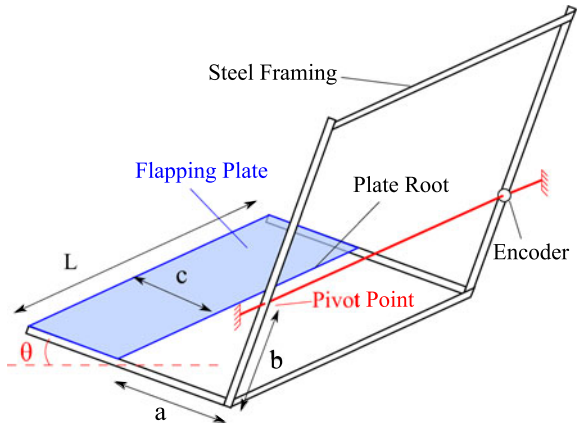

Fig. 4. Diagram illustrating the disturbance generator used in this experiment.

respectively. The plate has a chord length of 609 mm (24 in) and a span of 1.8 m (72 in). The flat plate has a sufficiently long span so that the AUV experiences a uniform wave along its length, and the disturbance can be largely isolated to the heave and sway directions, reducing the dynamics to a 2D problem. It should be noted that due to the rigid disturbance generator geometry, the heave and pitch amplitudes of the flapping plate oscillation, A_h and A_θ are coupled. More specifically, their relationship is given by $A_\theta = cA_h/(a-b)$; therefore, throughout the rest of the paper we will describe a given flapping motion by the heave amplitude A_h, and the pitch amplitude can be determined from this correlation.

The disturbance generator pivot point is rigidly attached to the platform extending across the vehicle testing tank, and the oscillations are created by manually swinging the lever. For this study we look at two general classes of disturbances, large-amplitude low-frequency disturbances, and small-amplitude high-frequency disturbances. The AUV attempting to maintain steady position under these disturbances should be functionally similar to behavior in the *cruising* and *docking regimes* described in Section II-B, respectively. Since the disturbance generator is operated by hand, the disturbances cannot be repeated exactly, but effort was taken to maintain a sufficient

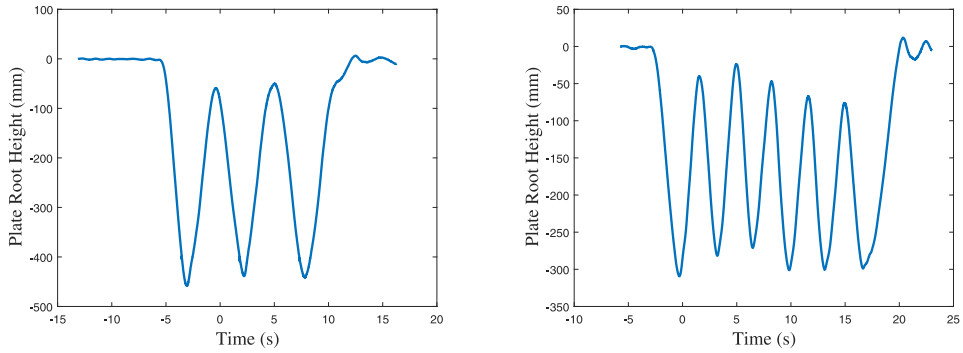

Fig. 5. Representative examples of the different disturbance generator oscillations for this study. (a) The height of the flat plate for a high-amplitude low-frequency disturbance, and (b) the height of the plate for the low-amplitude high-frequency disturbance.

TABLE I
SUMMARY OF THE DIFFERENT TESTING CONDITIONS AND DISTURBANCE PARAMETERS

Case	Control	n	A_h	f
1	None	4	70 ± 35	0.37 ± 0.03
2	PID	4	83 ± 8	0.34 ± 0.03
3	None	4	184 ± 28	0.22 ± 0.03
4	PID	5	157 ± 23	0.20 ± 0.01

n is the number of trials for each case, A_h is the amplitude of the plate heaving oscillation (in mm), and f is the frequency of the oscillation (in Hz). The standard deviation of the trials is listed after the mean value for each parameter.

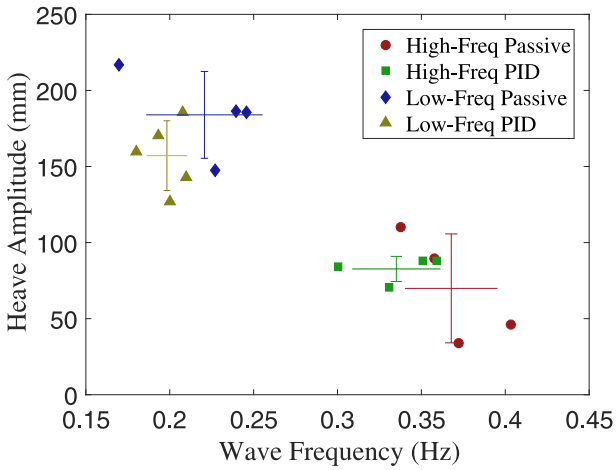

Fig. 6. The exact heaving amplitude and frequency of the disturbance generator for each test case. The tests contributing to case 1 are indicated by circle markers, those for case 2 by square markers, those for case 3 by diamond markers, and those for case 4 by triangular markers. The mean and standard deviation of each case is marked by intersecting error bars.

degree of consistency between the two types of disturbances. Table I summarizes the heaving amplitude as well as the dominant frequency component for each testing case providing the statistical distribution of different trials for each case. The variation in disturbance generator parameters for the different trials is also shown graphically in Fig. 6. As representative examples for the different types of disturbances, the pitching height of the flat plate is shown as a function of time for both a high and

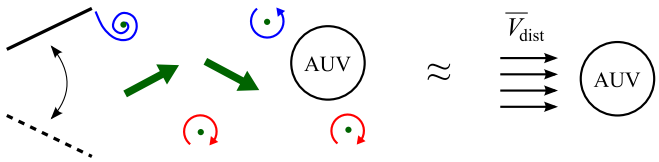

Fig. 7. A schematic diagram of the flow field created by the flapping plate of the wave generator. The flow is approximated by a reverse Karman vortex street. A vortex street is a repeating array of vortices of strength γ and vertical and horizontal spacing h_{VS} and a_{VS}, respectively.

low frequency disturbance in Fig. 5. As is indicated in Table I, some cases use PID feedback control and some have no control at all. This is so that we have a reference for how much the passive vehicle moves with the waves to compare with the position tracking stability under feedback control.

The flow created by flapping foils has been the subject of numerous studies as it relates to flutter in aircraft [21] and both aquatic and aerial biological propulsion [22]. When a flat plate accelerates through a fluid, the shear layer extending into the surrounding fluid forms one or more horseshoe vortices in each flapping direction. The complex interaction between these vortices and their evolution can be difficult to model. However, we have designed the plate of the disturbance generator to have a span of 1.8 m, so that it extends well beyond the front and back of CephaloBot. In this region, the flow can be generally described by a 2D reverse Karman vortex street [21], which is depicted on the left side of Fig. 7. The vortex street is characterized by the vertical spacing h_{VS}, horizontal spacing a_{VS}, and vortex strength γ.

Obviously the flow associated with the reverse Karman vortex street varies with both position and time, so there is no single disturbance velocity that can be associated with a given set of disturbance generator parameters A_h and f. However, the translational velocity of the vortices will provide a velocity scale as a function of the flapping frequency and amplitude. The translational velocity of vortices in a vortex street is given by [23],

$$V_{\text{trans}} = \frac{\gamma}{2a_{\text{VS}}} \tanh\left(\frac{\pi h_{\text{VS}}}{a_{\text{VS}}}\right). \tag{5}$$

The translational velocity must also be equal to the product of horizontal spacing and flapping frequency, $V_{\text{trans}} = a_{\text{VS}} f$.

Utilizing this fact, and assuming that the vertical vortex spacing is proportional to the total heaving amplitude, $h_{\text{VS}} = C_1 A_h$, we can show that the vortex strength is proportional to the following vorticity scale, $\gamma = C_\gamma A_h^2 f$ where $C_\gamma = C_1^2/k^2 \tanh(\pi k)$. Here k is the ratio of of the vortex street spacing $k = h_{\text{VS}}/a_{\text{VS}}$. We will not require the vortex street to be stable ($k \approx 0.28$) given how close the AUV is to the disturbance generator, we will however assume that this ratio is constant for different cases. Plugging these relationships back into (5) we show that the translational velocity is proportional to a similar velocity scale, $V_{\text{trans}} = C_V A_h f$, where $C_V = C_1/2k$.

We relate V_{trans} to an equivalent steady disturbance velocity, $\bar{V}_{dist}$, by assuming that the average force in the sway direction is steady, $\bar{V}_{dist}$, (see the right side of Fig. 7), and correlating drag forces determined from tracked motion of the vehicle to the disturbance velocity through previously measured drag coefficients. The disturbance velocity should be proportional to the same velocity scale,

$$\bar{V}_{dist} = C_{\text{VD}} A_h f \,, \tag{6}$$

and the coefficient C_{VD} is fitted empirically using the passive (no control) cases 1 and 3, and hydrodynamic coefficients for the vehicle determined in [19]. Typical governing dynamic models for marine vehicles characterize hydrodynamic forces in terms of drag and added mass as functions of relative fluid velocity and acceleration respectively [24]. In the sway direction this can be summarized by,

$$(m + A_{22})\,\dot{v} + D_{22} v = F_y \,, \tag{7}$$

where m is the vehicle mass, v is the relative sway velocity, F_y is the total thruster control force, and A_{22} and D_{22} are dimensional added mass and drag coefficients in the sway direction. These coefficients were measured and validated for CephaloBot at typical operating speeds as $A_{22} = 1.97$ kg and $D_{22} = 21.05$ kg/s in [19]. When the first wave impacts the vehicle its velocity will be small compared to the disturbance velocity, so the drag/disturbance force can be considered constant. By measuring the sway distance traveled by the AUV, Δy_1, over the period of the first wave, Δt_1, during cases 1 and 3 where $F_y = 0$, the equivalent steady disturbance velocity can be calculated as,

$$\bar{V}_{dist} = \frac{2\,(m + A_{22})\,\Delta y_1}{D_{22} \Delta t_1^2} \,. \tag{8}$$

We used this relationship to calculate $\bar{V}_{dist}$ during cases 1 and 3 and then calibrated C_{VD}, inserting the heave amplitude and frequency of each test into (6).

IV. Results

A. Disturbance Velocity

As was discussed in Section III-B, basic scaling analysis suggests that an equivalent steady disturbance velocity is proportional to the velocity scale, $A_h f$, and the coefficient C_{VD} can be calibrated using the vehicle trajectory data during the passive/no-control cases. Fig. 8 shows $\bar{V}_{dist}$, calculated from (8), with respect to the velocity scale, $A_h f$, for each test in cases 1 and 3. Using this data, we have calculated $C_{\text{VD}} = 27.18$ as the best linear fit to the data, which is shown in Fig. 8.

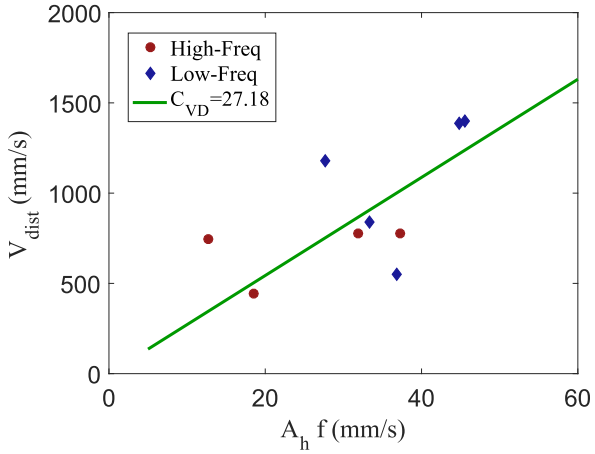

Fig. 8. The equivalent steady disturbance velocity, $\bar{V}_{dist}$, calculated from (8), is shown as a function of the disturbance velocity scale, $A_h f$, confirming an approximately linear proportionality between the two.

TABLE II
SUMMARY OF VEHICLE TRACKING STABILITY PERFORMANCE

Case	Mean Y-error (mm)	RMS Y-error (mm)
1	636	763
2	196	218
3	984	1156
4	190	201

Mean $Y - error$ is the first order mean of the sway position tracking error and RMS Y-error is the root mean square of the sway error.

The data in Fig. 8 converges fairly well on this linear trend, at least qualitatively validating the assumption that the different tests have similar vortex street ratios, k, and heave separation coefficients, C_1. This also validates the derivation that the velocity scale, $A_h f$, correlates with the disturbance force/velocity. It can also be observed from Fig. 8 that the test cases have equivalent steady disturbance velocities ranging from ≈3–6 body diameters a second.

B. Position Tracking Stability

The AUV described in II is tracked using an underwater motion capture system while it responds to wave disturbances in the sway direction generated as described in III. In order to characterize the station keeping abilities using bioinspired thrusters under different types of disturbances, we first record the passive vehicle response to the disturbances, and then compare that to the position tracking stability under feedback control. For each case, the wave disturbance parameters are described in Table I. The mean and RMS sway errors averaged over all the tests for each case are summarized in Table II.

The position tracking stability of the AUV/thruster system, for the large-amplitude low-frequency disturbances is illustrated by Fig. 9. This figure shows the trajectory of the vehicle averaged over all the tests for both cases 3 and 4. For all tests, the instant

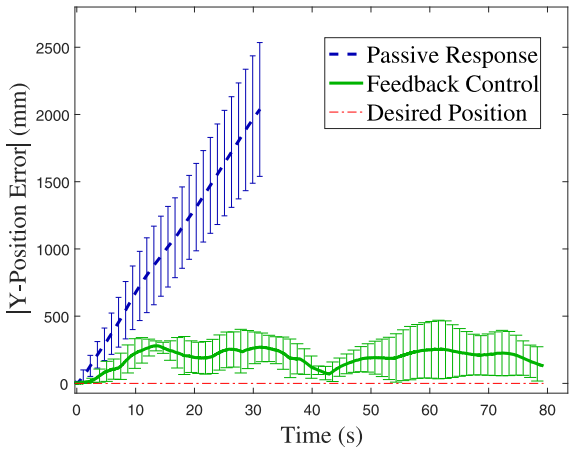

Fig. 9. Sway position error of the AUV when it encounters a high amplitude low-frequency wave-disturbance. The passive response of the vehicle is shown by the dashed line, while the position tracking error under PID control is shown by the solid line. The error bars indicate the standard deviation between the different trials.

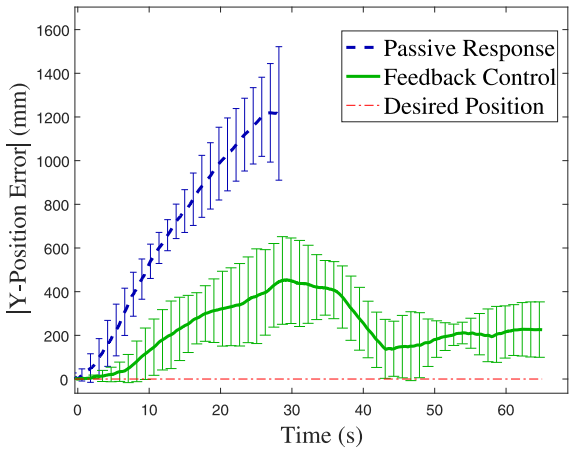

Fig. 10. Sway position error of the AUV when it encounters a low-amplitude high-frequency wave disturbance. The passive response of the vehicle is shown by the dashed line, while the position tracking error under PID control is shown by the solid line. The error bars indicate the standard deviation between the different trials.

the vehicle encounters the initial disturbance wave, time is set to $t = 0$. The error bars indicate the standard deviation between the different tests in each case. It can be seen from this figure that, as would be expected, the position tracking error is much lower for the cases with feedback control, demonstrating the capability of the bioinspired propulsion to handle high-amplitude low-frequency disturbances. The amplitude of the feedback control rms position error is 17% of the passive test drift and is on the order of the vehicle diameter. The reason that the position error for the uncontrolled cases is tracked for a shorter period of time than the controlled tests, is because the vehicle is pushed out of the motion capture measurement zone.

The position tracking stability for the low-amplitude high-frequency tests are illustrated in Fig. 10. As can be seen in this figure the bioinspired propulsion is also capable of performing station keeping in the presence of high frequency disturbances which are troublesome to traditional propeller thrusters. The rms

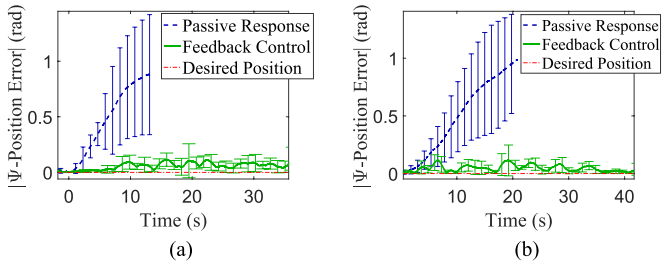

Fig. 11. Yaw position error of the AUV when it encounters (a) a high amplitude low-frequency wave-disturbance, and (b) a low amplitude high frequency wave-disturbance. The passive response of the vehicle is shown by the dashed line, while the position tracking error under PID control is shown by the solid line. The error bars indicate the standard deviation between the different trials.

position error of the control test is 28% of the uncontrolled case. Although this is a larger percentage of the passive sway error, the absolute tracking error is nearly equivalent to the high amplitude cases. This suggests that the observed tracking error may be limited by the PID control scheme, rather than thruster settling times. Furthermore it should be noted that the frequency of the disturbance for case 2 is 0.34 Hz, meaning that it successfully handles the disturbances even though the disturbance frequency is higher than the control bandwidth for oscillating maneuvers in the *docking* regime. This is due to the fact that driving vehicle maneuvers at that frequency requires overcoming vehicle inertia; whereas disturbance rejection requires overcoming the hydrodynamic forces. For low-amplitude high-frequency disturbances the hydrodynamic forces may be small in comparison to inertial forces. As such the control bandwidth for disturbance rejection is going to be much higher than the maneuvering control bandwidth in this regime. The high control bandwidth of the bioinspired thruster technology makes it ideal for these small-scale high-frequency disturbances.

As a general note, we'd like to point out that CephaloBot has by far the largest surface area and coefficient of drag in the sway direction. Since disturbances during open water testing will rarely line up exactly in this direction, The component of disturbance velocity in the max drag direction will be reduced. Therefore it is reasonable to expect a similar performance for larger waves, in practice.

The disturbances cause forces predominantly in the sway direction, but the testing is performed on an unconstrained AUV, so any small shift in the yaw angle will make subsequent disturbances non-uniform, amplifying the yaw angle error. We have also included the heading angle error for all cases in Fig. 11(a) and (b). For the uncontrolled cases, any small error is amplified until the vehicle reaches a heading of $\Psi = \pm\pi/2$, which has a minimized area with respect to the incoming wave and is hence a stable position. For the controlled cases, very little energy is required to maintain the desired heading, and does so easily.

C. Comparison With Other AUVs

Lawrance *et al.* [25] report the position tracking performance of a Seabotix vLBV300 observation-class ROV using PID feedback control during an ocean deployment with wave disturbances measuring as high as 700 mm in amplitude which

is about 40% larger than the oscillation of the flat plate tip (combination of heaving and pitching) for the low-frequency disturbances. The ROV in this study has a mass of 19 kg which is very similar to the 20 kg mass of CephaloBot. That study observed mean tracking errors in the sway direction of 145 mm and rms errors at 191 mm, which are comparable to the errors of our vehicle utilizing bioinspired propulsion. Similarly, Kim *et al.* [26] report sway position rms error of 82 mm for an AUV using PD control in waves generating 15 N sinusoidal sway forces at a frequency of 0.10 Hz, which is comparable to our vehicle response to large amplitude waves. That AUV, called Cyclops, has a mass of 219 kg, and dimensions of $1477 \times 868 \times 920$ mm, so it is significantly larger than CephaloBot, and performed the position tracking in a test basin with a wave generator consisting of multiple thrusters. Fischer *et al.* report that the AUV SubjuGator has sway position errors of 92 mm in the presence of waves 0.5–1.25 m in height [10], using a non-linear RISE-controller. This AUV has a mass of 38 kg and measures $381 \times 558 \times 558$ mm, and testing was performed in the gulf of Mexico.

V. Conclusion

In this letter, we show that our novel, biologically inspired squid thrusters are able to match the performance of traditional propellers for hydrodynamic disturbance rejection, without impacting the vehicle forward drag. We integrated the squid thrusters into our AUV, CephaloBot, in a configuration such that they provide decoupled control authority over the sway and yaw dynamics of the vehicle. We developed and presented a model of the vehicle and actuators; from this model, a PID controller was developed to perform a station-keeping maneuver in the presence of hydrodynamic disturbances. To experimentally validate our actuators and controller, a wave generator was constructed and placed in our testing facility. A motion capture system was used to localize the vehicle and disturbance generator. Several sets of data were collected in the presence of both low frequency, high amplitude and high frequency, low amplitude waves. The data compares favorably with other state-of-the-art underwater vehicles being used in research applications.

References

[1] G. S. Triantafyllou, M. S. Triantafyllou, and M. A. Grosenbaugh, "Optimal thrust development in oscillating foils with application to fish propulsion," *J. Fluids Struct.*, vol. 7, no. 2, pp. 205–224, 1993. [Online]. Available: http://dx.doi.org/10.1006/jfls.1993.1012

[2] X. Tan, "Autonomous robotic fish as mobile sensor platforms: Challenges and potential solutions," *Mar. Technol. Soc. J.*, vol. 45, no. 4, pp. 31–40, 2011.

[3] S. B. Behbahani and X. Tan, "Design and modeling of flexible passive rowing joints for robotic fish pectoral fins," *IEEE Trans. Robot.*, vol. 32, no. 5, pp. 1119–1132, Oct. 2013.

[4] K. Mohseni, "Pulsatile vortex generators for low-speed maneuvering of small underwater vehicles," *Ocean Eng.*, vol. 33, no. 16, pp. 2209–2223, 2006. [Online]. Available: http://dx.doi.org/10.1016/j.oceaneng.2005.10.022

[5] M. Krieg, P. Klein, R. Hodgkinson, and K. Mohseni, "A hybrid class underwater vehicle: Bioinspired propulsion, embedded system, and acoustic communication and localization system," *Mar. Technol. Soc. J., Special Ed. Biomimetics Mar. Technol.*, vol. 45, no. 4, pp. 153–164, 2011. [Online]. Available: http://dx.doi.org/10.4031/MTSJ.45.4.11

[6] D. Yoerger and J. J. E. Slotine, "Adaptive sliding control of and experimental underwater vehicle," in *Proc. IEEE Int. Conf. Robot. Autom.*, Sacramento, CA, USA, Apr. 9–11, 1991, pp. 2746–2751. [Online]. Available: http://dx.doi.org/10.1109/ROBOT.1991.132047

[7] A. J. Healey, S. M. Rock, S. Cody, D. Miles, and J. P. Brown, "Toward an improved understanding of thruster dynamics for underwater vehicles," in *Proc. Auton. Underwater Veh. Technol.*, Cambridge, MA, USA, Jul. 19–20 1994, pp. 340–352.

[8] G. Antonelli, S. Chiaverini, N. Sarkar, and M. West, "Adaptive control of an autonomous underwater vehicle: Experimental results on ODIN," *IEEE Trans. Control Syst. Technol.*, vol. 9, no. 5, pp. 756–765, Sep. 2001. [Online]. Available: http://dx.doi.org/10.1109/87.944470

[9] G. Antonelli, F. Caccavale, S. Chiaverini, and L. Villani, "Tracking control for underwater vehicle-manipulator systems with velocity estimation," *IEEE J. Ocean. Eng.*, vol. 25, no. 3, pp. 399–413, Jul. 2000. [Online]. Available: http://dx.doi.org/10.1109/48.855403

[10] N. Fischer, D. Hughes, P. Walters, E. M. Schwartz, and W. E. Dixon, "Nonlinear rise-based control of an autonomous underwater vehicle," *IEEE Trans. Robot.*, vol. 30, no. 4, pp. 845–852, Aug. 2014.

[11] M. Krieg and K. Mohseni, "Dynamic modeling and control of biologically inspired vortex ring thrusters for underwater robot locomotion," *IEEE Trans. Robot.*, vol. 26, no. 3, pp. 542–554, Jun. 2010. [Online]. Available: http://dx.doi.org/10.1109/TRO.2010.2046069

[12] S. P. Colin and J. H. Costello, "Morphology, swimming performance and propulsive mode of six co-occuring hyromedusae," *J. Exp. Biol.*, vol. 205, pp. 427–437, 2002.

[13] I. K. Bartol, P. S. Krueger, W. J. Stewart, and J. T. Thompson, "Hydrodynamics of pulsed jetting in juvenile and adult brief squid *Lolliguncula brevis*: Evidence of multiple jet 'modes' and their implications for propulsive efficiency," *J. Exp. Biol.*, vol. 212, no. 12, pp. 1889–1903, 2009. [Online]. Available: http://dx.doi.org/10.1242/jeb.027771

[14] M. Krieg and K. Mohseni, "Modelling circulation, impulse and kinetic energy of starting jets with non-zero radial velocity," *J. Fluid Mech.*, vol. 719, pp. 488–526, 2013. [Online]. Available: http://dx.doi.org/10.1017/jfm.2013.9

[15] M. Krieg and K. Mohseni, "Pressure and work analysis of unsteady, deformable, axisymmetric, jet producing cavity bodies," *J. Fluid Mech.*, vol. 769, pp. 337–368, 2015. [Online]. Available: http://dx.doi.org/10.1017/jfm.2015.120

[16] P. Krueger, J. Dabiri, and M. Gharib, "The formation number of vortex rings formed in a uniform background co-flow," *J. Fluid Mech.*, vol. 556, pp. 147–166, 2006. [Online]. Available: http://dx.doi.org/10.1017/S0022112006009347

[17] W. J. Pierson and L. A. Moskowitz, "Proposed spectral form for fully developed wind seas based on the similarity theory of S. A. Kitaigorodskii," *J. Geophys. Res.*, vol. 69, no. 24, pp. 5181–5190, 1964. [Online]. Available: http://dx.doi.org/10.1029/JZ069i024p05181

[18] M. K. Ochi and E. N. Hubble, "Six-parameter wave spectra," in *Proc. 15th Int. Conf.* Proc. *Coastal Eng. 1976*, 1977, pp. 301–328.

[19] M. Krieg and K. Mohseni, "Comparison of different methods for estimating energetics related to efficiency on a UUV with cephalopod inspired propulsion," in *Proc. Int. Symp. Mar. Propulsors*, Helsinki, Finland, Jun. 12–15, 2017, pp. 32–42.

[20] Y. Xu and K. Mohseni, "Bio-inspired hydrodynamic force feed forward for autonomous underwater vehicle control," *IEEE/ASME Trans. Mechatronics*, vol. 19, no. 4, pp. 1127–1137, Aug. 2013. [Online]. Available: http://dx.doi.org/10.1109/TMECH.2013.2271037

[21] M. Koochesfahani, "Vortical patterns in the wake of an oscillating airfoil," *AIAA J.*, vol. 27, no. 9, pp. 1200–1205, 1989. [Online]. Available: http://dx.doi.org/10.2514/6.1987-111

[22] M. S. Triantafyllou, G. S. Triantafyllou, and D. K. P. Yue, "Hydrodynamics of fishlike swimming," *Annu. Rev. Fluid Mech.*, vol. 32, pp. 33–53, 2000. [Online]. Available: http://dx.doi.org/10.1146/annurev.fluid.32.1.33

[23] P. G. Saffman, *Vortex Dynamics*. Cambridge, U.K.: Cambridge Univ. Press, 1992.

[24] T. I. Fossen, *Guidance and Control of Ocean Vehicles*. Hoboken, NJ, USA: Wiley, 1994.

[25] N. R. J. Lawrance, T. Somers, D. Jones, S. McCammon, and G. A. Hollinger, "Ocean deployment and testing of a semi-autonomous underwater vehicle," in *Proc. MTS/IEEE OCEANS*, Monterey, CA, USA, Sep. 2016, pp.–1–6.

[26] J. Kim, H. Joe, S. C. Yu, J. S. Lee, and M. Kim, "Time-delay controller design for position control of autonomous underwater vehicle under disturbances," *IEEE Trans. Ind. Electron.*, vol. 63, no. 2, pp. 1052–1061, Feb. 2016.